Synergy effect in the photocatalytic degradation of textile dyeing waste water by using microwave combustion synthesized nickel oxide supported activated carbon

P. Suresh[a], J. Judith Vijaya[a,*], T. Balasubramaniam[a], L. John Kennedy[b]

[a]*Catalysis and Nanomaterials Research Laboratory, Department of Chemistry, Loyola College, Chennai 600 034, Tamilnadu, India,*
Tel. +91 44 28178200; Fax: +91 44 28175566; emails: innocentsuresh@yahoo.co.in (P. Suresh),
jjvijayaloyoal@yahoo.co.in, jjvijaya78@gmail.com (J.J. Vijaya), balache08@gmail.com (T. Balasubramaniam)
[b]*Materials Division, School of Advanced Sciences, VIT University, Chennai Campus, Chennai 600 048, Tamilnadu, India,*
Tel. +91 44 39931555; email: jklsac14@yahoo.co.in

ABSTRACT

Nickel oxide nanoparticles supported activated carbon (NSAC) photocatalyst was successfully prepared using a cost-effective microwave irradiation method. The earned UV light-sensitive NSAC composites were characterized using powder X-ray diffraction, Fourier transform infrared spectroscopy, High-resolution scanning electron microscope with energy-dispersive X-ray analysis, X-ray photoelectron spectroscopy, and Brunauer–Emmett–Teller surface area analyzer. Optical properties of NSAC composites were investigated using UV–Vis diffuse reflectance spectroscopy and photoluminescence spectroscopy, which exposed prolonged light absorption in UV light region and hold better charge separation capability, respectively, as compared to pure NiO. The photocatalytic activity was tested by the degradation of textile dye waste water (TDW) under UV light irradiation. Chemical oxygen demand of TDW was calibrated before and after the photocatalysis experiment under UV light to evaluate the mineralization of wastewater. The results demonstrated that NSAC composites showed imposing photocatalytic enrichment over pure NiO. The coordinated blending of the oxygen vacant sites, structural defects of NiO along with electron transmission capacity, and presence of surface oxygen on AC has led to the lasting light absorption, delayed charge recombination, and sustenance, which favor the enrichment of the photocatalytic activity of NSAC.

Keywords: Photocatalytic degradation; NiO nanoparticles; Activated carbon; Synergy effect

1. Introduction

Textile industries are one of the groups of industries stimulating intense water pollution. The textile wastewaters consist of diverse chemical products, marked levels of organic compounds and they have precarious pH, high chemical oxygen demand (COD), reduced biological demand, and immense colorization [1]. Textile wastewaters are highly injurious to natural areas and can be very dangerous to the environmental life. The high organic matter content results in depletion of dissolved oxygen, which has an adverse effect

*Corresponding author.

on the marine ecological system and the whole ecosystem [2].

The textile effluent is defined by the high COD. The textile industries are creating constant efforts to reduce the COD level, by innumerable methods, such as hydrolysis in a basic medium, chemical processes, membrane filtration, biological treatment, and foam flotation [3–5]. Eventhough these methods were inadequate for the highly toxic textile wastewaters [6].the advanced oxidation processes like photocatalysis, Fenton, and photo-Fenton have been employed in the handling of textile wastewater [7–9].

Amidst numerous treatment processes employed to treat the textile dyeing effluents, heterogeneous photocatalysis emerges as the best, because it is a cost-effective treatment process [10–13]. In the previous decade, many metal oxide semiconductors like TiO_2, ZnO, and NiO were used as heterogeneous photocatalysts. NiO is a p-type semitransparent semiconductor, with a wide band gap between (3.6 eV) valence band (3.1 eV) and conduction band (−0.5 V) with a weak absorption bands in the visible region that makes it applicable for photocatalytic processes [14–19].

NiO was used for the degradation of crystal violet, 4-chlorophenol, 2,4-dichlorophenol, in the photocatalytic degradation of Congo red dye from aqueous solutions, and in the photocatalytic bleaching of rose bengal [20–22]. But, due to its limitation factor of high percentage of electron–hole recombination, and practical difficulties, exploration is still going on for NiO composite material [23].

New investigations have shown that the photocatalytic efficiency of TiO_2 and ZnO increased to a large extent, when it was supported by the activated carbon [24]. Activated carbon (AC) support gives rise to a cheaper and effective waste water treatment [25]. The dominant influence of AC would be its high adsorption capability, which can aid to enrich the organic substrate around the catalyst, stimulate the pollutant transfer process, and thus increase the photocatalytic efficiency [26–29]. It can also increase the life time of electron–hole pairs and promote the target reactions [30]. The mode of synergistic effect of adsorption by AC and photocatalytic decomposition by TiO_2 and ZnO has been studied in the degradation of several types of organic pollutants [31–34].

In the present work, we focused on the preparation and characterization of pure NiO and NiO- supported activated carbon (NSAC) composite catalysts by microwave combustion synthesis. There are many methods available to impregnate NiO onto the carbon surface, but solution combustion synthesis is a productive method for the fabrication of NiO onto the carbon support [35]. Also, the microwave-assisted combustion synthesis is environment friendly, rapid, and cost-effective, and the resultant NiO nanoparticles are pure [36].

The influence of carbon support on NiO photocatalytic efficiency was investigated from the degradation of textile dyeing waste water under UV light irradiation. The as-prepared novel NSAC exhibited extended UV light absorption and greater adsorptivity of textile dye and enhanced photocatalytic activity than pure NiO.

Prior to this study, there has been no attempt made to prepare nickel oxide-supported AC by microwave combustion synthesis, and also no literature is found on the use of NSAC for the degradation of textile dyeing waste water.

2. Materials and methods

2.1. Preparation of NSAC

NSAC was prepared by using the following procedure. An AC prepared from rice husk by two-stage, two-step activation process was employed as a support material [37].

Nickel nitrate hexahydrate and urea of analar grade (Merck, India) were used as the precursors for the synthesis of NSAC. Stoichiometric amounts of nickel nitrate hexahydrate and urea were dissolved separately in 10 mL of distilled water. Liquefied urea was added to aqueous nickel nitrate hexahydrate solution. To this mixture, 1 g of AC was added, and stirred for 5 h. The mixture obtained was heated in a microwave (2.45 GHz, 750 W) for 10 min. The product was washed with distilled water, and dried in a hot air oven at 100°C for 1 h and is labeled as NSAC. Five samples of NSAC were prepared with varying the NiO loading from 10 to 50%. The samples were labeled as NSAC1, NSAC2, NSAC3, NSAC4, and NSAC5. The pure NiO was also prepared by using the same procedure, without adding the carbon base for comparison purpose.

2.2. Characterization of NSAC

The crystallinity of AC and NSAC was analyzed by using a Philips X'pert X-ray diffractometer for 2θ values ranging from 10 to 80˚ using Cu Kα radiation at λ = 1.540 Å. A Perkin-Elmer infrared spectrometer was utilized for analyzing the functional groups on the surface of the samples in the spectral range of 4,000–400 cm^{-1}. Morphological analysis and energy-dispersive X-ray analysis were done using a Jeol JSM6360 high-resolution scanning electron microscope. Diffused reflectance spectroscopy on powder samples were carried out in a Cary100 UV–Visible spectrophotometer to estimate the

band gap energy of the samples as reported in [38]. The photoluminescence properties of the nanostructures were recorded by using a Varian Cary Eclipse Fluorescence spectrophotometer. The specific surface area and porosity were evaluated from the surface area and a porosity analyzer (ASAP 2020 V3.00H, Micromeritics Instrument Corp., Norcross, GA).

2.3. Photocatalytic reactor setup and the degradation procedure

The photocatalytic degradation of textile dyeing waste water (TDW) obtained from the dyeing industry, Tiruppur, Tamilnadu, India was carried out in a multi-lamp photocatalytic reactor. The reactor contains the low-pressure mercury lamps (8/8 W) emitting 365 nm UV radiation, which is sufficient for the photocatalytic degradation of TDW. The TDW was taken in glass reactor tubes, which can hold 100 mL of the dye solution. The procedure to study the photocatalytic degradation study is of the following sequence. The mineralization of TDW was obtained by measuring the decrease of COD of the waste water. COD of TDW was determined before and after the photocatalytic treatment with a standard dichromate method using a COD digester. The known initial COD of the TDW was taken and to it known weight of NSAC or pure NiO were added. It was kept in dark for 12 h to reach the adsorption equilibrium, and the resultant COD was calculated. This solution was taken in the photocatalytic reactor and UV irradiation was supplied for 2 h. At regular interval of 20 min, equal aliquot was removed from the reactor tube, centrifuged, and the COD was estimated to measure the extent of TDW degradation. The percentage of COD removal was calculated from the formula,

$$\% \text{ removal of COD (mg/L)} = (\text{initial COD - final COD/initial COD}) \times 100$$

(1)

Indian pollution control board standard has fixed that the let-out TDW from the textile industries into the river bodies must have only 250 mg/L COD, and hence the photocatalytic degradation of TDW was carried out using NSAC to degrade it to 250 mg/L COD.

3. Results and discussion

3.1. X-ray diffraction analysis

The AC and NSAC samples were analyzed by X-ray diffraction (XRD) in the range of 2θ between 10° and 80°. The corresponding XRD pattern of the AC

and NSAC (1–5) are shown in Fig. 1. The existence of peaks at 2θ angles 44.51°, 51.85°, and 76.36° are accounted for the presence Ni and they correspond to (1 1 1), (2 0 0), and (2 2 0) planes, respectively (JCPDS 4-850, Face-centered cubic phase). While the peaks at 2θ angles 37.24°, 43.27°, 62.85°, 75.43°, and 79.48° can be indexed as (1 1 1), (2 0 0), (2 2 0), (3 1 1), and (2 2 2) crystal planes of NiO, respectively. These planes of NiO are then linked with d-spacing standards of 2.40, 2.08, 1.47, and 1.24 Å, appropriately. The results obtained from the characteristic diffraction peaks are in good agreement with the standard NiO data (JCPDS file No. 4-835) having cubic phase.

In AC, two peaks at 2θ angles of 23° and 29° correspond to the presence of silica in the carbon matrix. AC showed a broad peak at 2θ angle of 22°, which accounts for the presence of mineral SiO_2, and a small peak at 2θ angle of 44° was obtained for (0 1 0) plane of graphitic structure [39]. The presence of portion of silica was also identified for all the NSAC samples by the EDX analysis. This implies that silica which is one of the main constituent of the precursor is not expelled completely from carbon matrix even at high temperature that is liberated during microwave
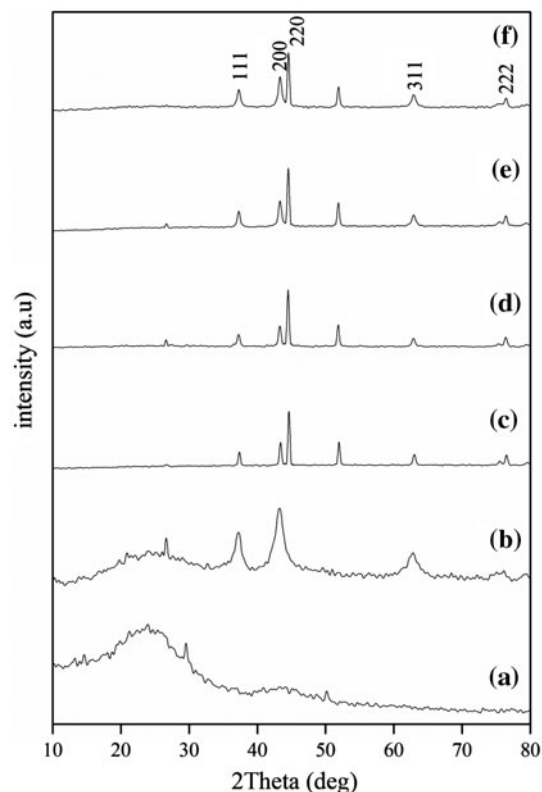
Fig. 1. XRD patterns of (a) AC, (b) NSAC1, (c) NSAC2, (d) NSAC3, (e) NSAC4 and (f) NSAC5.

irradiation. The intensity of the graphitic peak at 44° decreased drastically in NSAC, which may be due to the NiO nanostructures formation on the AC matrix. The existence of graphite in AC will play a decisive role in the growth mechanism of NSAC.

The crystallite size of NSAC samples was estimated by using Scherer's equation [40].

$$L = \frac{0.9\lambda}{\beta cos\theta} \tag{2}$$

where λ is the X-ray wavelength θ, Bragg diffraction angle and β, peak width at full-width half-maximum. Among the peaks, we selected the strongest peak (200) at $2\theta = 43.27°$ to calculate the crystallite size. The estimated crystallite sizes of NSAC (1–5) samples are 27.91, 21.32, 17.96, 15.77, and 13.67 nm, respectively. It was observed that the crystallite size decreases with an increase in NiO loading.

The growth of NiO and Ni nanoparticles on the surface of AC is possible due to appropriate growth mechanism. The main assistance is the exorbitant amount of heat liberated within a short duration of time due to microwave irradiation. The growth mechanism may involve three steps, such as combustion synthesis of NiO, carbothermal reduction of NiO to Ni-rich vapors/ions, and re-oxidation of Ni-rich vapors/ions to NiO nanoparticles [41]. The combustion synthesis that could have taken place inside the microwave oven is enumerated as follows [42]:

$$\begin{aligned} &Ni(NO_3)_2 \cdot 6H_2O_{(s)} + CO(NH_2)_{2(s)} + O_{2(g)} \\ &\quad \rightarrow NiO_{(s)} + 8H_2O_{(g)} \uparrow + CO_{2(g)} \uparrow + N_{2(g)} \uparrow + 2NO_{2(g)} \uparrow \end{aligned}$$
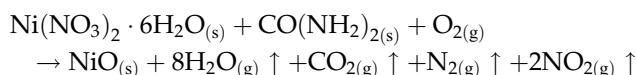
In combustion process, nickel nitrate hexahydrate acts as an oxidizing agent and urea is the fuel employed. The sustenance of high temperature in a combustion synthesis leads to confined heating of reactant mixture, higher discharge rate of gas evolvement, and limited interparticle coercion. These factors play a decisive role in the formation of NiO nanoparticles on the surface of AC. Further, carbothermal reduction of NiO to Ni-rich vapor/ions takes place. Ma et al. [43] have studied the carbothermal reduction of ZnO into Zn-rich vapors in the presence of carbon/ graphite at 900°C temperature. Carbon/graphite in AC and enormous amount of heat present in the microwave oven becomes favorable for the carbothermal reduction of ZnO into Zn-rich vapors/ions. Cheng et al. [44] have also found that Ni-rich vapors/ions could be reduced to nanosized Ni particles with amorphous carbon as reducing agent at 500°C. Titirici et al.

[45] reported that the nickel nitrate could be decomposed to nickel oxide at 300°C and metal Ni at 500°C. Sharma et al. [46] displayed that micron-sized NiO particles could be reduced by natural graphite at 950°C. Hattori et al. [47] exhibited that amorphous carbon plays an important role in the prevention of the Ni nanoparticles from aggregation and oxidation, because surface-active sites for oxidation of the metallic Ni particles are terminated by carbon atoms. So a part of the Ni-rich vapors/ ions are reduced to Ni nanoparticles and the rest is further reoxidized to NiO nanoparticles by CO/CO_2, which are abundantly present within the microwave oven. Thus, NiO and Ni nanoparticles are incorporated onto AC matrix.

3.2. Fourier transform infrared (FT-IR) analysis

The infrared spectra of the prepared materials AC and NSAC (1–5) are shown in Fig. 2. The presence of a weak band at 3,753 cm^{-1} can be referred to the confined O–H groups in the prepared samples. A broad peak at 3,427 cm^{-1} is due to the stretching vibration of hydroxyl groups of H_2O and the H–OH bending
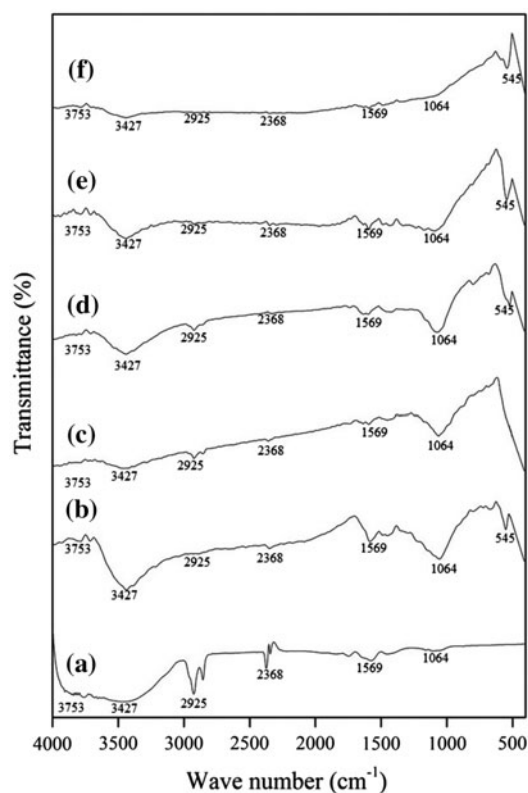
Fig. 2. Fourier transform infrared (FT-IR) spectra of (a) AC, (b) NSAC1, (c) NSAC2, (d) NSAC3, (e) NSAC4 and (f) NSAC5.

vibration emerge at $1,615\,cm^{-1}$ [48,49]. FTIR results show an escalation in the concentration of hydroxyl groups on the surface of NSAC samples, which foster not only the capturing of electrons to strengthen the separation ability of electrons–holes, and also the inception of the surface free radicals to increase the photocatalytic degradation efficiency [50].

In AC, a sharp, intense band at $2,925\,cm^{-1}$ is attributed to the asymmetric C–H stretching vibrations of alkanes. However, in NSAC (1–5) samples, the intensity of these two bands has diminished exceptionally. This is an indication that the microwave generates the high temperature, which leads to the partial loss of the particular functional groups in NSAC.

A band near $2,368\,cm^{-1}$ is due to the C≡C vibration of the alkyne groups. The band at $1,569\,cm^{-1}$ is assigned to the C=C vibrations of alkenes and aromatic functional groups. This band is profound in NSAC samples, which may be due to the increase in the concentration of the corresponding functional groups. A band at around $1,438–1,412\,cm^{-1}$ is assigned to the in-plane deformation of CH_2 group. This band intensity has increased considerably for NSAC samples. The peak at $1,064\,cm^{-1}$ is resulted from the overlap of several bands, including the absorption due to the vibration modes of CH_2OH and the C–O stretching vibration coupled to the C–O bending mode of cell carbohydrates [51]. All the samples show an important band at $1,045\,cm^{-1}$ corresponding to Si–O–Si stretching, and this may be due to the presence of silica in the carbon matrix. The absorption band at $545\,cm^{-1}$ in NSAC samples indicates the presence of in-plane vibration of hydrogen-bonded hydroxyl group [52]. The NSAC (1–5) samples show strong band at $420\,cm^{-1}$ equivalent to the stretching vibration of Ni–O. It implies that the NiO nanospheres are successfully anchored onto the carbon support [53].

3.3. Morphology of pure NiO and NSAC

HR-SEM micrographs of pure NiO and NSAC (1–5) are shown in Fig. 3(a–f). HR-SEM images show that the nanoparticles are spherical and they are agglomerated. Since the samples are prepared by combustion synthesis in a microwave burning, independent, homogenous growth of nanostructures are not feasible. The production of nanoparticles cannot be guarded in a combustion synthesis, due to the liberation of high amount of heat, and this always produces particles with differing sizes. As a consequence, the HR-SEM images of pure NiO show that the particle sizes range from 15 to 60 nm, and for NSAC samples, it ranges from 18 to 130 nm. Fig. 3(a) displays the presence of NiO nanoparticles on the walls and within

pores of the activated carbon. In Fig. 3(b), NiO nanosphere-like structures are present on the walls of the pores, and on the surface of the carbon support, but they are sparsely distributed, due to the lesser loading of NiO. Fig. 3(c) reveals the increase in NiO loading, on the carbon support. Fig. 3(d) shows the presence of more and larger sized NiO on the surface of the carbon support, and they are of bigger nanospheres. Fig. 3(e) unfolds the enormous amount of NiO nanospheres uniformly distributed on the carbon support. Fig. 3(f) displays the clusters of pure NiO nanosphere-like structure, which are agglomerated to a certain extent.

The elemental analysis of NSAC (1–5) samples is characterized by a X-ray energy-dispersive spectrometer (EDX). Fig. 4(a–e) depicts the EDX patterns of the NSAC samples. On careful investigation, the samples contain only the elements of C, O, Si, and Ni. The weight percentage of Ni shows a steady increase from NSAC1 to NSAC5, which is in coherence with NiO loading onto to the carbon support. On the other hand, the weight percentage of C decreases from NSAC1 to NSAC5. The existence of silica in all the samples indicates that the silica is not fully removed from the carbon support even at high temperature liberated in microwave heating.

3.4. XPS analysis

X-ray photoelectron spectroscopy (XPS) analysis has been executed to find out the possible NiO structure on the carbon support in NSAC. The XPS spectra of NSAC is illustrated in Fig. 5(a), which indicated the existence of carbon, oxygen, silica, and nickel on the carbon matrix and this is in good agreement with the EDX results.

Fig. 5(b) shows the profile of Ni 2p electron, a doublet of the Ni $2p_{3/2}$ and $2p_{1/2}$ peaks from the Ni^{2+} states, which are at 855.1 and 873.3 eV, respectively, as well as their corresponding shake-up resonances at 861.1 and 880 eV. These peaks are assigned to oxidized nickel in a dispersed phase [54], and they confirm the presence of Ni^{2+} in NSAC [55–59]. But, there is a shift of the Ni $2p_{3/2}$ and $2p_{1/2}$ peaks to the higher energy in NSAC, which is assigned to the anchoring of Ni into the carbon matrix, and the resultant formation of NiO. It also results in the charge transfer from Ni^{2+} to the carbon matrix.

Fig. 5(c) shows the O1s core-level spectra of NSAC. Deconvolution of the O1s peak gives two components at 531 and 532.9 eV. The peak at 531 eV implies the adsorbed oxygen on the vacancy sites of NiO samples, and it is associated with the O^- sublattice, and further
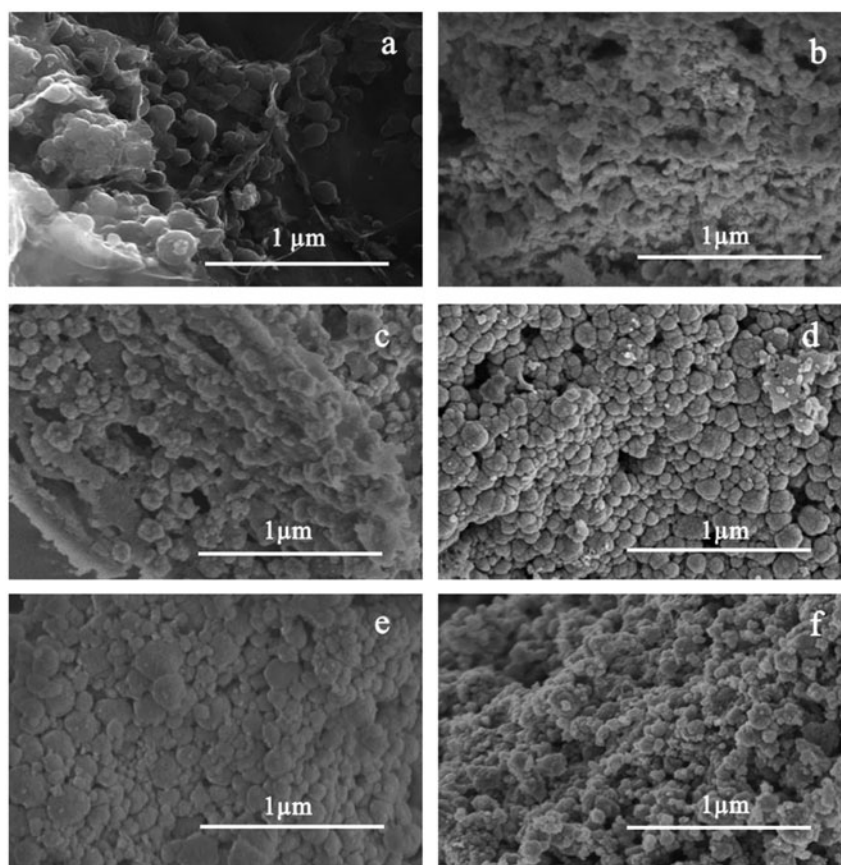
Fig. 3. HR-SEM images of (a) NSAC1, (b) NSAC2, (c) NSAC3, (d) NSAC4, (e) NSAC5 and (f) pure NiO.

it corresponds to the carbonyl oxygen atoms [60]. The peak at 532.9 eV affirms the presence of carbonyl oxygen atoms in esters, amides, and anhydrides, as well as oxygen atoms in hydroxyls or ethers [61]. Additionally, it signifies NiO lattice oxygen deficiency, and the surface-bonded O–H or O_2 [62]. Besides, the binding energy of O 1s region showed an increase up to 532.9 eV for NSAC as compared to 530.97 eV for pure NiO, as reported in the literature [63]. The increase in the binding energy may be due to the capture of Ni on carbon surface and the surface interaction between C at Ni atoms [64].

The high-resolution XPS spectra of the C 1s region is exhibited in Fig. 5(d), and the peak at 284.1 eV match the sp^2 carbon bonding in graphitic carbon. The peak at 289 eV is attributed to the carbonyl, quinine groups, lactone, or ester groups [65]. Moreover, an extra peak at high binding energy at about 294 eV is attributed to $\pi \rightarrow \pi^*$ transitions [66]. It can also be referred to C=C–O surface group [67–69]. Thus, the existence of NiO on the carbon matrix is confirmed by XPS studies.

3.5. Optical studies

3.5.1. Diffuse reflectance spectroscopy studies

The diffuse reflectance spectra of pure NiO and NSAC (1–5) samples in the range of 200–800 nm were investigated to establish the optical absorption properties of the photocatalyst samples. The results are shown in Fig. 6, which show the presence of broad absorption bands in the range of 200–300 nm (6.2–4.1 eV). The bands of NSAC (1–5) were of higher energy, when compared to pure NiO. The NSAC (1–5) samples displays higher optical absorption; this is due to addition of intermediate energy bands in NSAC (1–5), and these intermediate energy levels decrease the effective band gap of the NiO and make it more receptive in the UV region of the electromagnetic spectrum. Fig. 7 presents UV/VIS reflectance spectra of AC and NSAC (1–5) displaying the optical properties of the samples.

The reflectance spectra were analyzed using a modified Kubelka–Munk function $F(R)$, estimated from the following equation [70]:
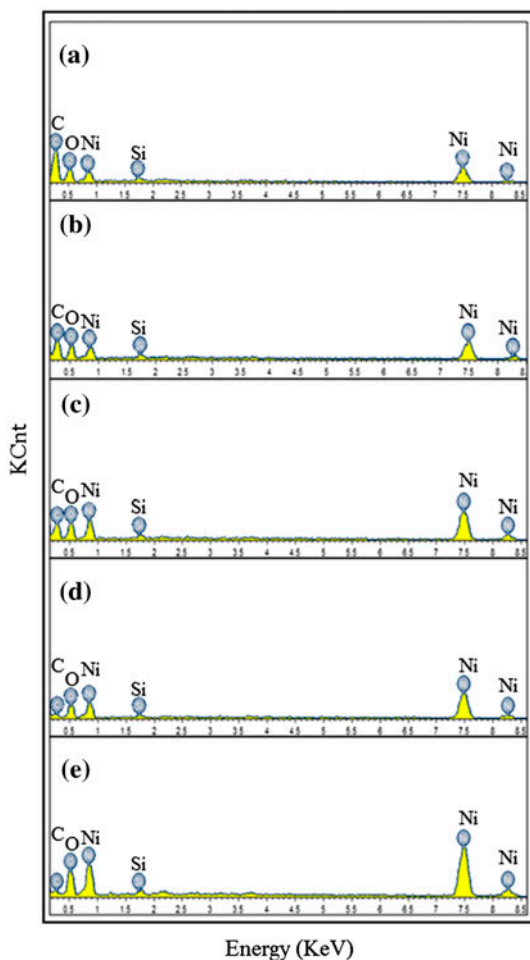
Fig. 4. EDX analysis of (a) NSAC1, (b) NSAC2, (c) NSAC3, (d) NSAC4 and (e) NSAC5.

$$F(R) = (1 - R)^2/2R \qquad (3)$$

$F(R)$ is the Kubelka–Munk function, where R is the reflectance. A graph was plotted between $[F(R)h\upsilon]^2$ and $h\upsilon$, and the intercept value obtained corresponds to the band gap energy. The band gaps of pure NiO, and NSAC (1–5) were evaluated by using the modified Kubelka–Munk function as shown in Fig. 8. The calculated band gaps for pure NiO, AC, and NSAC (1–5) are 3.52, 4.13, 3.45, 3.43, 3.36, 3.43, and 3.42 eV, respectively. The diffuse reflectance spectra results clearly show that the samples are probable photocatalyst, which can perform efficiently under UV radiation.

3.5.2. Photoluminescence studies

The photoluminescence (PL) spectra of NSAC (1–5) and pure NiO excited at 330 nm at room temperature are shown in Fig. 9. NSAC samples show an intense PL peak at around 433 nm (2.86 eV) and two broad peaks at 459 nm (2.70 eV) and 485 nm (2.56 eV), whereas the pure NiO show a strong peak at 361 nm (3.43 eV). In NiO crystal structure, the Ni^{2+}ions fill the tetrahedral sites coordinated by four oxygen atoms. Due to the microwave synthesis of NiO nanostructures, structural distortion could have been taken place in the crystal structure. This structural irregularity in NiO give rise to the intra-band gap or the energy levels between the valence and conduction band, and they give rise to the defect emissions. The intra-bands are formed, due to the fast evaporation, partial oxidation, and rapid crystallization that happen during the microwave heating. These PL peaks distinctly manifest that these bands are not because of the band gap emission, but they are the consequence of structural defects, such as oxygen vacancies. The oxygen vacancies on the surface of NiO samples would favor the O_2 adsorption, and consecutive production of O_2 radical groups, which brings about the oxidation of organic materials [71]. Thus, NSAC samples with structural defects and oxygen vacancies on their surface would be the potential photocatalysts for the degradation of textile effluents.

3.6. BET analysis

The porous structure of NSAC (1–5) was studied by using nitrogen adsorption at 77 K, and compared with the AC. The nitrogen isotherms of AC and NSAC (1–5) samples are plotted in Fig. 10(a–f). The surface area parameters are reported in Table 1. The pore diameter (D_p) for the AC is 1.89 nm, while the average pore diameter for the NSAC is 3.71 nm. It can be seen from Table 1 that the surface area of the AC is much larger than the NSAC, implying that NiO loading onto carbon matrix reduces the porosity and makes it less porous material. Similarly, the pore volume of the NSAC (1–5) samples is smaller than the AC.

The isotherm of AC, and NSAC (1–5), carry a round knee at relative pressure of $0.05 < P/Po < 0.15$, thus indicating the presence of wider micropores. They also exhibit hysteresis loop, corresponding to the mesopore structure behavior of Type-IV isotherm. Thus, the AC and NSAC (1–5) samples are a blend of Type-I and Type-IV isotherms as defined by IUPAC classification. AC uptake of nitrogen adsorption reached as high as 136.63 cm^3/g, whereas lowest nitrogen adsorption of 33.47 cm^3/g was obtained for NSAC5. The specific BET surface area of the sample decreased from 446.44 to 36.92 m^2/g with an increase in NiO loading.
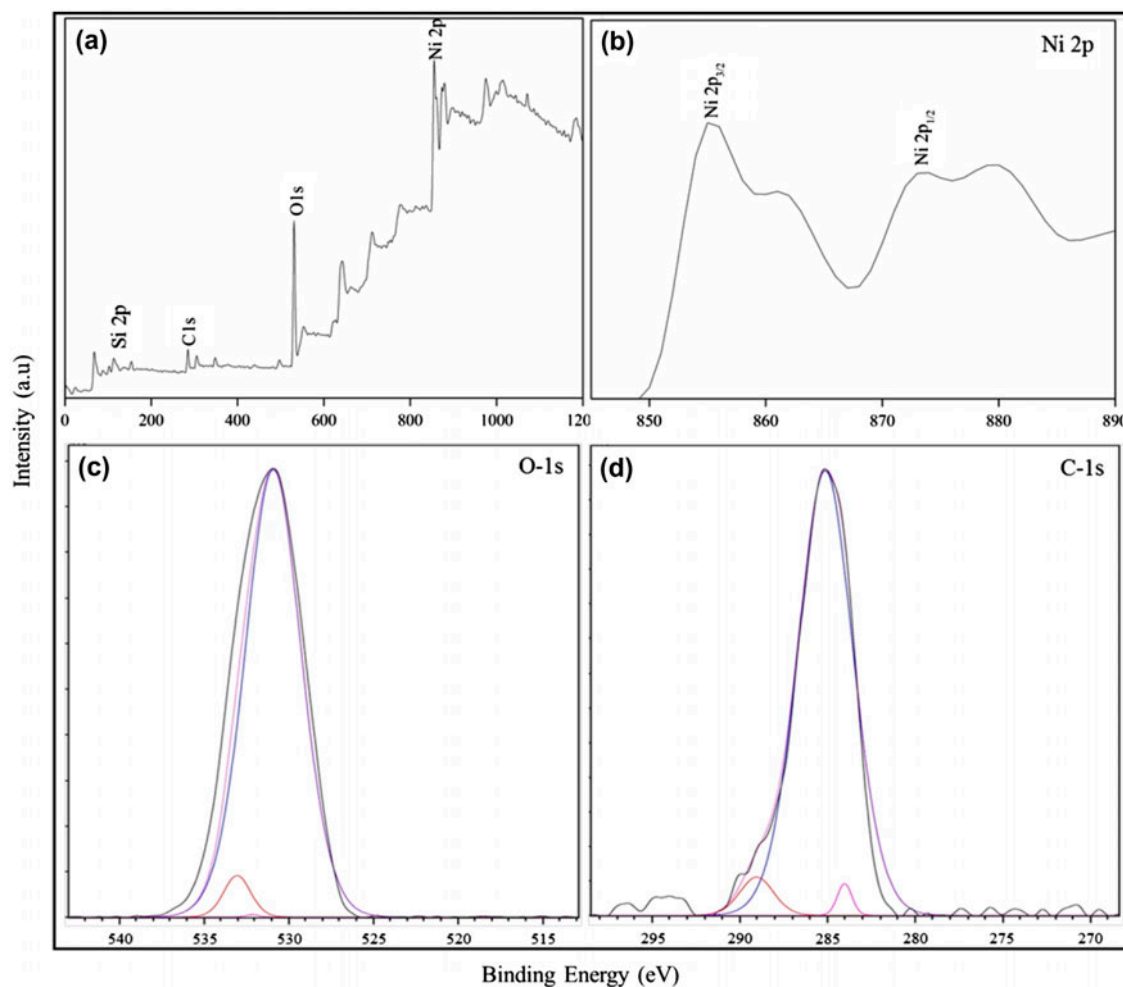
Fig. 5. XPS spectra of NSAC5 a) Wide spectra, b) Ni-2p, c) O-1s and d) C-1s.
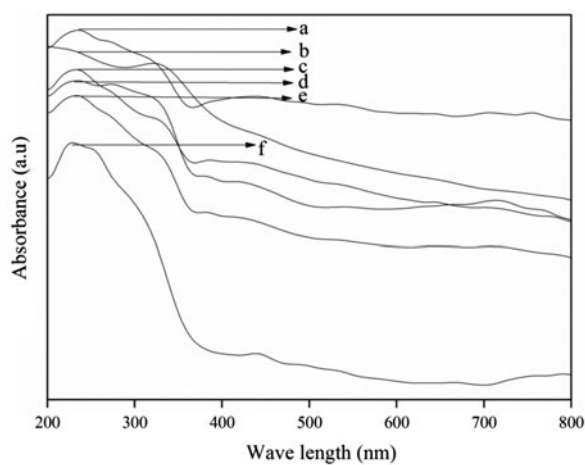
Fig. 6. UV–visible absorbance of (a) pure NiO, (b) NSAC1, (c) NSAC2, (d) NSAC3, (e) NSAC4 and (f) NSAC5.
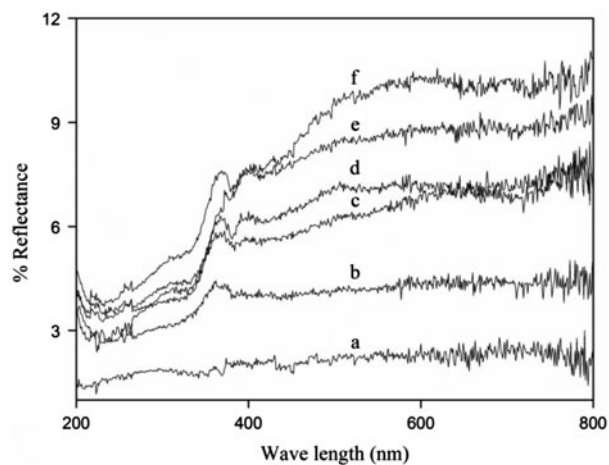
Fig. 7. UV/VIS reflectance spectra of (a) AC, (b) NSAC1, (c) NSAC2, (d) NSAC3,(e) NSAC4 and (f) NSAC5.
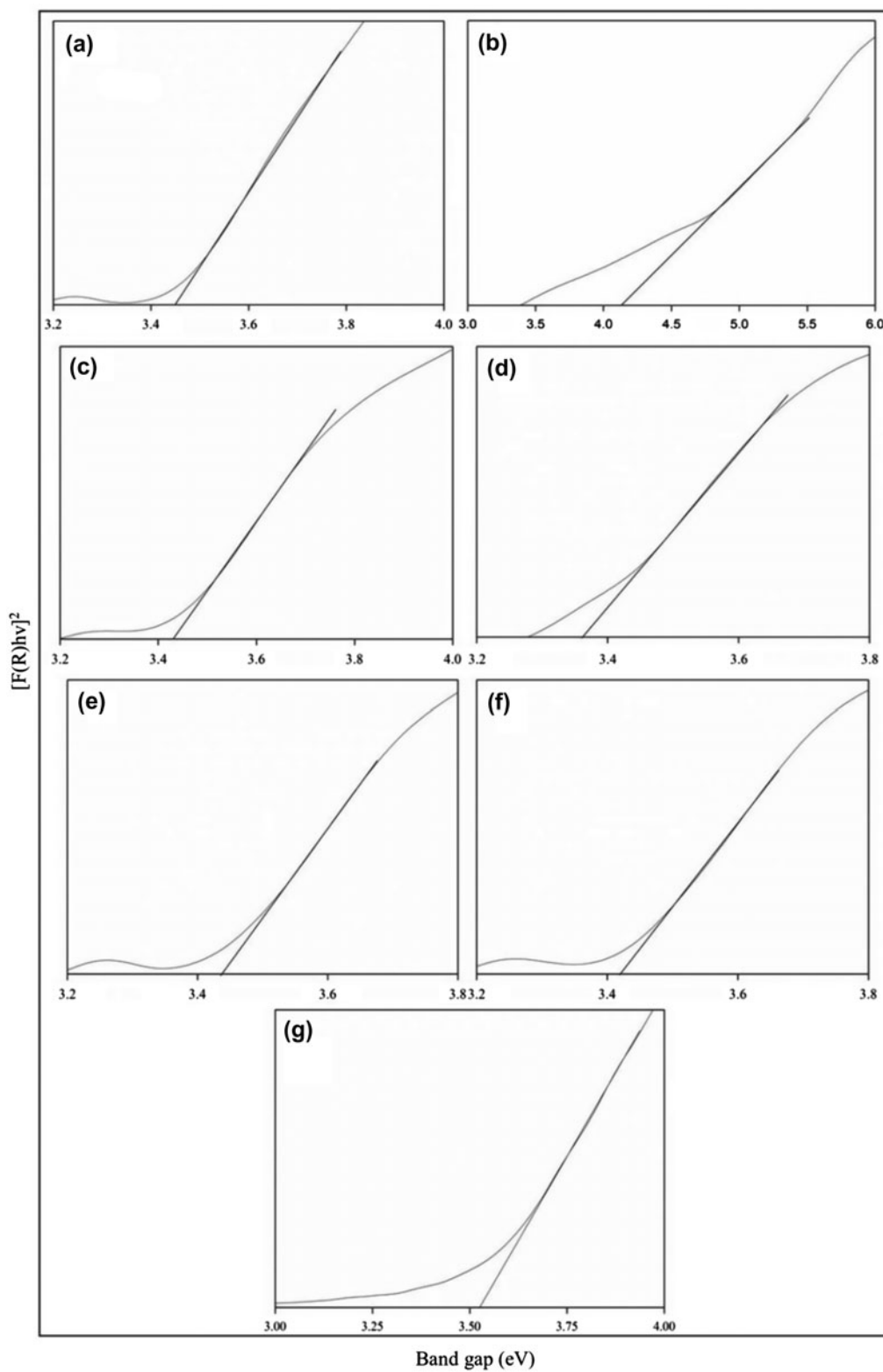
Fig. 8. Kubelka–Munk plots of (a) pure NiO, (b) AC, (c) NSAC1, (d) NSAC2, (e) NSAC3, (f) NSAC4 and (g) NSAC5.
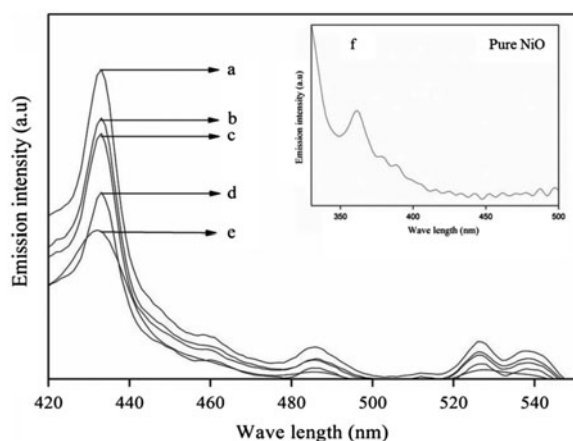
Fig. 9. Room-temperature PL spectra of (a) NSAC1, (b) NSAC2, (c) NSAC3, (d) NSAC4, (e) NSAC5 and (f) pure NiO.
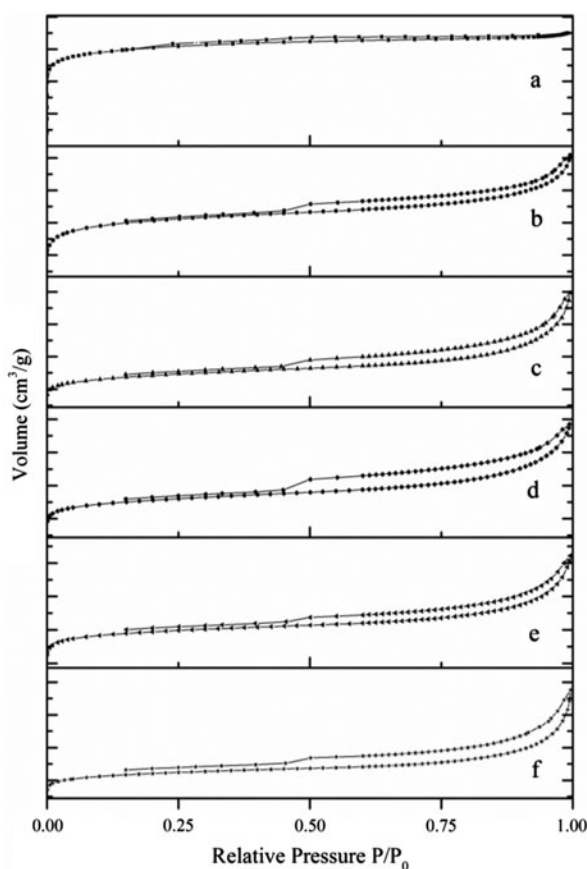
Fig. 10. Nitrogen adsorption/desorption isotherm of (a) AC, (b)NSAC1, (c) NSAC2, (d) NSAC3, (e) NSAC4 and (f) NSAC5.

3.7. Photocatalytic activity

An initial study of the photocatalytic degradation of TDW (850 mg/L COD) with NSAC (1–5) catalysts is carried out and their photocatalytic ability is determined from their COD removal efficiency of the TDW under UV light irradiation. COD removal confirms the destruction of the organic materials in the TDW and the color reduction [64]. The percentage of COD removal obtained for NSAC (1–5) samples are: 35.7, 40.3, 46.1, 54.5, 61.3, and 70.1%, respectively, for 120 min irradiation. The NSAC5 catalyst was found to be the most efficient one. Hence, NSAC5 is studied for the various experimental parameters and its photodegradability efficiency is tested with pure NiO.

The COD removal of TDW using AC, NSAC5, and pure NiO are studied by changing the amount of the catalyst form 50 to 1,000 mg. Fig. 11 illustrates the COD removal efficiency of AC, NSAC5, and pure NiO. The results show a linear increase in the photodegradation efficiency with an increase in the catalyst amount.

The photocatalytic efficiency of NiO is lower than that of NSAC5. In the photocatalytic degradation of TDW by NiO, an electron in an electron-filled valence band (VB) is excited by UV irradiation to a vacant conduction band (CB), leaving a positive hole in the VB. These electrons and positive holes drive the reduction and oxidation, respectively, of the compounds adsorbed on the surface of a photocatalyst. Bai et al. [63] attributed the NiO photocatalytic oxidation of toluene to the lattice oxygen on the surface of NiO. Pan et al. [72] highlighted the hierarchical and porous surface structures as a reason for the NiO photocatalytic degradation of acetaldehyde. Hameed et al. [73] emphasized electron–hole pair recombination inhibition in NiO–ZnO composite by charge transfer process, which has led to the photocatalytic degradation of MO. Song and Gao [74] studied the surface area of hollow NiO in their photocatalytic degradation of acid red 1 pollutant. Shang et al. [75] highlighted that the specific surface area, crystallinity, exposed facets, surface hydroxylation, surface defects, and surface adsorbability affect the photocatalytic activity of NiO. The oxygen vacant sites capture an excess electron, and as a result, this electron experiences a kind of attractive Madelung potential, which stabilizes them in the oxygen vacant site. The capturing of excess electrons increases its life span, which benefit the reaction of adsorbed molecules and its decay endows the increased photocatalytic activity.

The photocatalytic activity of AC is lower than that of pure NiO. But, AC is a semiconductor, and it favors the photocatalytic activity [76]. Gala et al. [77] studied

Table 1
Surface area parameters of AC and NSAC (1–5) samples

Sample	NiO loading (%)	S_{BET}[a] (m^2/g)	V_{Total}[b] (cm^3/g)	D_p[c] (nm)
AC	0	446.44	00.21	01.89
NSAC1	10	281.51	00.18	02.56
NSAC2	20	147.18	00.13	03.53
NSAC3	30	96.24	00.09	03.74
NSAC4	40	83.63	00.07	03.34
NSAC5	50	36.92	00.05	05.41

[a]BET surface area.
[b]Total pore volume.
[c]Pore diameter.
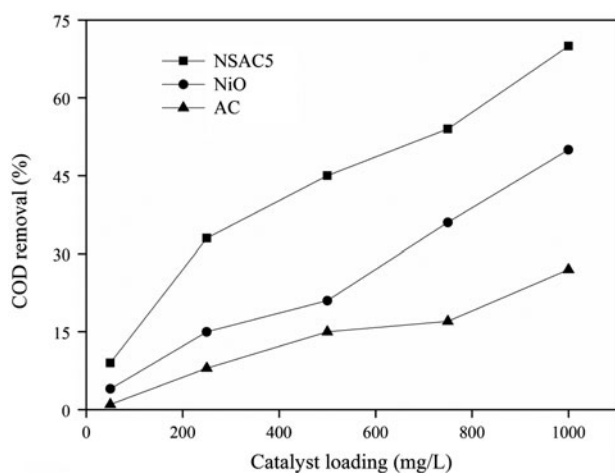
Fig. 11. Effect of catalyst loading on the photocatalytic degradation of TDW in the presence of AC, NSAC5 and NiO.

the E_g values of the activated carbons to prove them as the semiconductor materials with photoactivity in the presence of UV radiation. He also established a clear relationship between E_g values and the percentage of surface oxygen. Boehm [78] reported that when the photons from UV light falls on AC, it generates electron–hole pairs, due to the promotion of electrons from the valence band to the conduction band. The electrons advance throughout the sp^2 hybridized layers, and reach the molecules of the absorbed species and oxygen molecules. The electrons in turn reduce the adsorbed O$_2$ to set the superoxide radicals ($\cdot$O$_2^-$), which further reacts with the water molecule and initiates the generation of oxidizing radical groups that eventually degrades the organic matter. Besides the presence of adsorbed oxygen on AC surface that shuns the recombination of the electron with the positive hole, it also favors the interaction between the water molecule and the positive hole and thus expanding the capacity of the photocatalytic process.

The COD removal efficiency is extremely enhanced in NSAC5, due to the carbon support. The presence of AC as a support can act as a powerful electron transmission site, since it displays immense electrical conductivity, and large electron storage capacity, because of great specific surface area. Accordingly, the AC as support performed two important roles as an acceptor and transporter of propagated electrons of NiO and forcefully contained the charge recombination [79,80]. Additionally, due to the strong synergy between AC and NiO nanoparticles, the flow of propagated electrons amidst the AC and conduction band of NiO is increased. NiO is a good electron donor, and carbon materials are relatively good electron acceptors, the synergistic effect between these components effectively reduce the recombination leading to the increased charge carrier separation. The coordinated blending of the oxygen vacant sites, structural defects of NiO along with electron transmission capacity, and presence of surface oxygen on AC lead to lasting light absorption, delayed charge recombination, and sustenance which favor the enrichment of the photocatalytic activity of NSAC5 [81]. Gala et al. [77] studied the synergetic effect of W-supported activated carbon and discovered that the activated carbon with the higher percentage of surface oxygen, ester/anhydride groups, and carbon atoms with sp^2 hybridization would enhance the synergic activity of the activated carbon. Ahamad et al. have elaborately studied the role of CNT as support in ZnO-doped Cu system [64,82]. Kalid et al. [83] studied the synergetic effect of Fe and graphene on the photocatalytic efficiency of TiO$_2$.

The pH of the medium plays a vital role in the photocatalytic degradation processes of TDW, because pH affects the production of hydroxyl radical, which is a powerful oxidizing agent [84]. In order to determine the optimum pH, the pH of the solution was varied from 2.0 to 12 by adding appropriate amount

of NaOH or H_2SO_4 solutions. The results are presented in Fig. 12. It is observed that the maximum COD removal is possible in acidic medium, and 100% COD removal is obtained at pH 2 for NSAC5. However, NiO showed only 76% of COD removal at pH 2. And, the final pH after photo catalytic treatment is 7.25, which is a proof that the TDW was successfully degraded by the NSAC and the treated water can be the released into the water bodies. Hence, on the basis of results obtained pH 2 is chosen to be the optimum pH for photodegradation.

The point of zero charge (pHZPC) of NiO and NSAC5 are 7.85 and 8.90, respectively. The surface of the catalyst carries a net positive charge, when pH of the solution is below pHZPC, it would accelerate the adsorption of the negatively charged dyes molecules [85]. Similarly, when the medium becomes basic, hydroxide ions are easily adsorbed on the catalyst surface. Ion dipole hostility between the negatively charged catalyst surface and the negative charged dye molecules is reasonable at pH higher than the pHZPC [86]. This is the reason why TDW is showing lower photocatalytic degradation at higher alkalinity. Baransi et al. [87] observed similarly that at high pH, the forces of repulsion between the negatively charged TiO_2 catalyst surface and the organic species are increased, which results in a very low adsorption. Moreover, low degradation rate at higher pH is attributed to the fact that when the concentration of OH^- ion is higher in the solution, it prevents the penetration of UV light to reach the catalyst surface. Furthermore, high pH favours the formation of carbonate ions, which are effective scavengers of OH^- ions, and can reduce the COD removal rate [88].
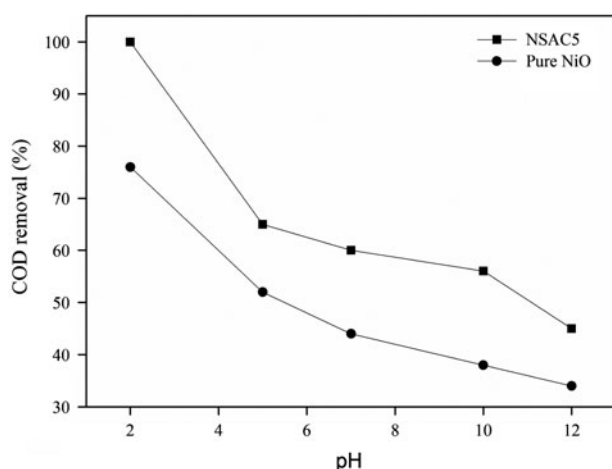
The factors that contribute the photocatalytic degradation at low pH are discussed as follows. The positive holes are considered as the major oxidation species at low pH. The lower pH produces more H^+ that could be adsorbed on the surface of NSAC5, thus making the catalyst positively charged. Positively charged NSAC5 particles assist the shift of photo-induced electrons, which could react with the adsorbed O_2 to produce $(\cdot O_2^-)$ $(e^- + O_2 \rightarrow \cdot O_2^-)$. In addition, positively charged NSAC particles could also inhibit the recombination of electrons and holes, generating more hydroxyl radical $(OH\cdot)$ through the reaction between the holes and water. Both the radical ions $\cdot O_2^-$ and OH**.** are strong oxidants, and could be responsible for the enhanced degradation of TDW [89]. Recently, Yoon and Lee [90] reported the adsorption onto TiO_2 at low pH, and the enhancement of electron–hole separation, which favor more positive holes to oxidize. Bayarri et al. [91] reported that at low pH values, the degradation takes place mainly through the reaction of adsorbed compounds with the photo-generated holes.

A kinetic study of the photocatalytic degradation of TDW for NiO and NSAC5 is also carried out. In order to obtain the kinetics of the photocatalytic degradation, the COD removal vs. irradiation time is plotted, which shows the formation of straight lines and indicate the zero-order reaction (Fig. 13). Zero-order reaction indicates that the rate is independent of the reactant concentration, i.e., the amount of dye molecule reacted is proportional to the time, the surface of NSAC reaches large amount of coverage by the TDW molecules, and the surface is fully saturated by the TDW molecules. Thus, the rate of the reaction does

Fig. 12. Effect of pH on the photocatalytic degradation of TDW in the presence of NSAC5 and NiO.
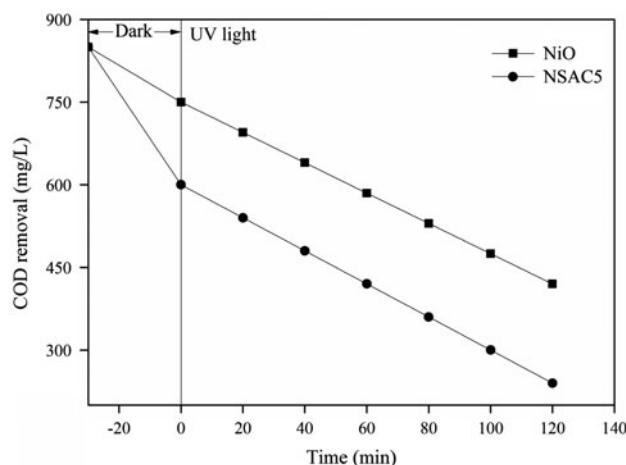
Fig. 13. Kinetic of TDW photocatalytic degradation for NSAC5 and NiO.
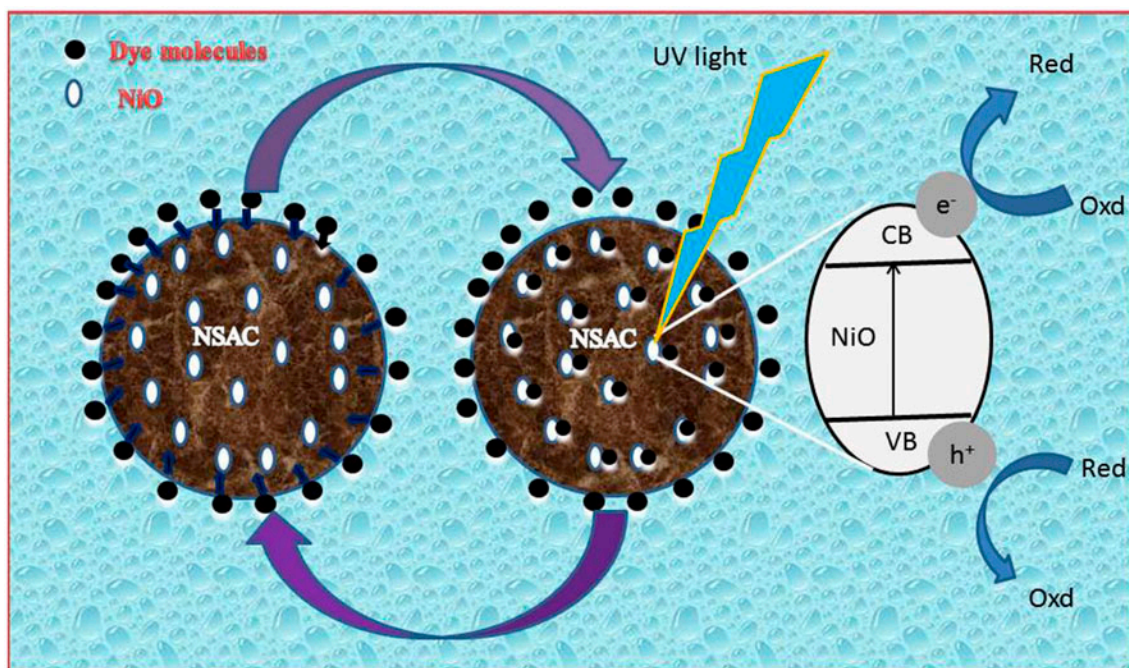
Fig. 14. Synergy mechanism on the surface of NSAC.

not depend anymore on the degree of coverage [92]. Mansouri et al. [93] reported the zero-order kinetics in the treatment of aqueous organics in the presence of TiO$_2$, Guerra et al. [79] investigated the zero-order kinetics in the degradation of reactive dyes in the presence of ZnO, and Foletto et al. [94] exposed zero-order kinetics in the use of ZnAl$_2$O$_4$ under sunlight. The rate constant for NiO and NSAC5 was 3.39 and 5.00 (mL^{-1} S^{-1}), respectively. The rate of photocatalytic degradation of NSAC5 is double than that of pure NiO. The synergy mechanism on the surface of NSAC5 is depicted in Fig. 14. AC with a wide surface area, high porosity, and various functional groups favors the preferential absorption of TDW on its surface and pores. As a consequence, the TDW molecules are further shifted to NiO surface, and degraded at a faster rate. The synergy effect between the carbon support and NiO is responsible for the enhancement in the photocatalytic efficiency of NSAC.

4. Conclusion

In summary, NiO nanospheres-supported activated carbon (NSAC) is successfully synthesized by microwave-assisted combustion synthesis with simple inorganic salts as raw materials. The XRD and XPS results confirm the presence of NiO on the carbon support. The uniform loading of NiO nanospheres on the carbon surface is revealed by HR-SEM images. The band gaps of the NSAC samples are in the range of 3.36–3.45 eV. NSAC samples are used for the photocatalytic degradation studies of TDW. Due to the synergetic effect, NSAC efficiency is higher than the pure NiO in effective and faster degradation of TDW.

References

[1] O.T. Can, COD removal from fruit-juice production wastewater by electro oxidation electro coagulation and electro-Fenton processes, Desalin. Water Treat. 52 (2014) 65–73.
[2] P. Kumar, R. Agnihotri, K.L. Wasewar, H. Uslu, C. Yoo, Status of adsorptive removal of dye from textile industry effluent, Desalin. Water Treat. 50 (2012) 226–244.
[3] B. Kus, M. Johir, J. Kandasamy, S. Vigneswaran, H. Shon, R. Sleigh, G. Moody, Performance of granular medium filtration and membrane filtration in treating storm water for harvesting and reuse, Desalin. Water Treat. 45 (2012) 120–127.
[4] S.B.A. Shammari, S.B. Hamad, A.A. Saffar, A.A. Sairafi, Efficiency of membrane bioreactor system in treating primary treated wastewater in Kuwait, Desalin. Water Treat. 36 (2011) 75–80.

[5] M. Mahmoud, A. Tawfik, F. Samhan, F.E. Gohary, Sewage treatment using an integrated system consisting of anaerobic hybrid reactor (AHR) and down flow hanging sponge (DHS), Desalin. Water Treat. 4 (2009) 168–176.

[6] B. Lodha, S. Chaudhari, Optimization of Fenton-biological treatment scheme for the treatment of aqueous dye solutions, J. Hazard. Mater. 148 (2007) 459–466.

[7] Y. Du, M. Qiu, Comparative study of advanced oxidation for textile wastewater, Desalin. Water Treat. 51 (2013) 5954–5958.

[8] P. Bansal, N. Bhullar, D. Sud, Studies on photodegradation of malachite green using TiO$_2$/ZnO photocatalyst, Desalin. Water Treat. 12 (2009) 108–113.

[9] M. Gao, G. Zhang, X. Wang, F. Yang, The bromamine acid removal from aqueous solution using electro-Fenton and Fenton systems, Desalin. Water Treat. 47 (2012) 157–162.

[10] S. Chen, Y. Yang, M. Ji, W. Liu, Preparation, characterisation and activity evaluation of CaCO$_3$/ZnO photocatalyst, Desalin. Water Treat. 6 (2011) 324–336.

[11] S. Chen, M. Ji, Y. Yang, W. Liu, Preparation and characterisation of AgIn(WO$_4$)$_2$ photocatalyst with high photoreduction activity, Desalin. Water Treat. 7 (2012) 98–108.

[12] W. Zhou, X. Yu, Use of Sr$_2$Bi$_2$O$_5$ as photocatalyst for the degradation of acid red G, Desalin. Water Treat. 30 (2011) 295–299.

[13] B. Amarsanaa, J.Y. Park, A. Figoli, E. Drioli, Optimum operating conditions in hybrid water treatment process of multi-channel ceramic MF and polyether sulfone beads loaded with photocatalyst, Desalin. Water Treat. 51 (2013) 5260–5267.

[14] D. Adler, J. Feinleib, Electrical and optical properties of narrow band materials, Phys. Rev. B. 2 (1970) 3112–3134.

[15] H. Sato, T. Minami, S. Takata, T. Yamada, Transparent conducting p-type NiO thin films prepared by magnetron sputtering, Thin Solid Films 236 (1993) 27–31.

[16] Y.M. Lu, W.S. Hwang, J.S. Yang, H.C. Chuang, Properties of nickel oxide thin films deposited by RF reactive magnetron sputtering, Thin Solid Films 420–421 (2002) 54–61.

[17] Y.N. Ju, J.R. Lead, Manufactured nanoparticles: An overview of their chemistry interactions and potential environmental implications, Sci. Total. Environ. 400 (2008) 396–414.

[18] D.H. Yang, C.S. Park, J.H. Min, M.H. Oh, Y.S. Yoon, S.W. Lee, J.S. Shin, Fullerene nano hybrid metal oxide ultrathin films, Curr. Appl. Phys. 9 (2009) 132–139.

[19] F. Augusto, E. Carasek, R.C.S. Gomes, S.R. Rivellino, A.D. Batista, E.A. Martendal, New sorbents for extraction and micro extraction techniques, J. Chromatogr. A. 1217 (2010) 2533–2542.

[20] F.C. Alina, M. Maria, M. Aurelia, Photocatalytic degradation of organic pollutants using NiO based materials, UPB Sci. Bull. Series B. 74 (2012) 109–116.

[21] F. Faezeh, H. Sara, Facile synthesis and characterization of nano porous NiO with folic acid as photodegradation catalyst for congo red, Mater. Sci. Appl. 3 (2012) 697–703.

[22] A. Pallavi, K. Anil, A. Rameshwar, R.K. Malkani, A comparative study of photocatalytic activity of some colored semiconducting oxides, Iran. J. Chem. Chem. Eng. 29 (2010) 43–48.

[23] R. Vinu, P. Sneha, M. Giridhar, Dye sensitized visible light degradation of phenolic compounds, J. Chem. Eng. 165 (2010) 784–797.

[24] G. Li Puma, A. Bono, D. Krishnaiah, J.G. Collin, Preparation of titanium dioxide photocatalyst loaded onto activated carbon support using chemical vapour deposition: A review paper, J. Hazard. Mater. 157 (2008) 209–219.

[25] M. Inagaki, T. Imai, T. Yoshikawa, B. Tryba, Photocatalytic activity of anatase powders for oxidation of methylene blue in water and diluted NO gas, Appl. Catal., B. 51 (2004) 247–254.

[26] Y. Li, M. Ma, S. Sun, X. Wang, W. Yan, Y. Ouyang, Preparation, photocatalytic activity of TiO$_2$–carbon surface composites by supercritical pretreatment and sol–gel process, Catal. Commun. 9 (2008) 1583–1587.

[27] Y. Li, S. Zhang, Q. Yu, W. Yin, The effects of activated carbon supports on the structure and properties of TiO$_2$ nanoparticles prepared by a sol–gel method, Appl. Surf. Sci. 253 (2007) 9254–9258.

[28] J. Xu, Y. Ao, D. Fu, C. Yuan, Synthesis of fluorine doped titania coated activated carbon under low temperature with high photocatalytic activity under visible light, J. Phys. Chem. Solids 69 (2008) 2366–2370.

[29] E. Carpio, P. Zu-niga, S. Ponce, J. Solis, J. Rodriguez, W. Estrada, Photocatalytic degradation of phenol using TiO$_2$ nanocrystals supported on activated carbon, J. Mol. Catal., A 228 (2005) 293–298.

[30] A. Subramani, K. Byrappa, S. Ananda, K. Lokanatha Rai, K. Lokanatha Rai, M. Yoshimura, Photocatalytic degradation of indigo carmine dye using TiO$_2$ impregnated activated carbon, Bull. Mater. Sci. 30 (2007) 37–41.

[31] J. Matos, J. Laine, J.M. Herrmann, D. Uzcategui, J.L. Brito, Influence of activated carbon upon titania on aqueous photocatalytic consecutive runs of phenol photodegradation, Appl. Catal., B. 70 (2007) 461–469.

[32] T.T. Lim, P.S. Yap, M. Srinivasan, A.G. Fane, TiO$_2$/AC composites for synergistic adsorption–photocatalysis processes: Present challenges and further developments for water treatment and reclamation, Crit. Rev. Environ. Sci. Technol. 41 (2011) 1173–1230.

[33] B. Tryba, A.W. Morawski, M. Inagaki, Application of TiO$_2$-mounted activated carbon to the removal of phenol from water, Appl. Catal., B. 41 (2003) 427–433.

[34] N. Sobana, B. Krishnakumar, M. Swaminathan, Synergism and effect of operational parameters on solar photocatalytic degradation of direct yellow 4 with AC-ZnO, Mater. Sci. Semicond. Process. 16 (2013) 1046–1051.

[35] S.T. Aruna, A.S. Mukasyan, Combustion synthesis and nanomaterials, Curr. Opin. Solid State Mater. Sci. 12 (2008) 44–50.

[36] Y. Koseoglu, A simple microwave assisted combustion synthesis and structural, optical and magnetic characterization of ZnO nano platelets, Ceram. Int. 40 (2014) 4673–4679.

[37] P. Suresh, J. Judith Vijaya, L. John Kennedy, R.T. Kumar, Two stage-two step activation process for the fabrication of micro-mesoporous carbons from rice husk, J. Bioprocess Eng. Biorefinery 2 (2013) 230–239.

[38] K. Sridharan, T.J. Park, Thorn-ball shaped TiO_2 nano-structures: Influence of Sn^{2+} doping on the morphology and enhanced visible light photocatalytic activity, Appl. Catal. B 134–135 (2013) 174–184.

[39] B. Sanjaya, J.R. Kalya, S. Srinivasarao, Rapid growth of nanotubes and nanorods of würtzite ZnO through microwave irradiation of a metalorganic complex of zinc and a surfactant in solution, Bull. Mater. Sci. 33 (2010) 89–95.

[40] B.D. Cullity, Elements of X-ray Diffraction. Addison-Wesley, Boston, MA, 1978.

[41] P. Suresh, J.J. Vijaya, L.J. Kennedy, Fabrication of hexagonal ZnO nanorods on porous carbon matrix by microwave irradiation, J. Nanosci. Nanotechnol. 13 (2013) 3068–3073.

[42] A. Manikandan, J.J. Vijaya, L.J. Kennedy, Comparative investigation of NiO nano- and microstructures for structural, optical and magnetic properties, Physica E 49 (2013) 117–123.

[43] H. Ma, J. Han, Y. Fu, Y. Song, C. Yu, X. Dong, Synthesis of visible light responsive ZnO–ZnS/C photocatalyst by simple carbothermal reduction, App. Catal. B. 102 (2011) 417–423.

[44] J. Cheng, X. Zhang, Y. Ye, Synthesis of nickel nanoparticles and carbon encapsulated nickel nanoparticles supported on carbon nanotubes, J. Solid State Chem. 179 (2006) 91–95.

[45] M.M. Titirici, A. Thomas, S.H. Yu, J.O. Muüller, M. Antonietti, A direct synthesis of mesoporous carbons with bicontinuous pore morphology from crude plant material by hydrothermal carbonization, Chem. Mater. 19 (2007) 4205–4212.

[46] S.K. Sharma, F.J. Vastola, P.L. Walker Jr., Reduction of nickel oxide by carbon: II. Interaction between nickel oxide and natural graphite, Carbon 35 (1997) 529–533.

[47] Y. Hattori, T. Konishi, H. Kanoh, S. Kawasaki, K. Kaneko, Stable nanoporous metallic nickel colloids, Adv. Mater. 15 (2003) 529–531.

[48] Z. Zhu, N. Wei, H. Liu, Z. He, Microwave assisted hydrothermal synthesis of $Ni(OH)_2$ architectures and their in situ thermal convention to NiO, Adv. Powder Technol. 22 (2011) 422–436.

[49] M.N. Salavati, M. Entesari, Controlled synthesis of spherical α-Ni $(OH)_2$ hierarchical nanostructures via a simple hydrothermal process and their conversion to NiO, Polyhedron 33 (2012) 302–313.

[50] Y.D. Hou, X.C. Wang, L. Wu, X.F. Chen, Z.X. Ding, X.X. Wang, X.Z. Fu, N-doped SiO_2/TiO_2 mesoporous nanoparticles with enhanced photocatalytic activity under visible light irradiation, Chemosphere 72 (2008) 414–421.

[51] O. Duggan, S.J. Allen, Study of the physical and chemical characteristics of a range of chemically treated, lignite based carbons, Water Sci. Technol. 35 (1997) 21–27.

[52] L.L. Teh, F.W. Wen, Y.S. Youn, T.L. Yi, B.W. Chen, Evaluation of microwave enhanced catalytic degradation of 4-chlorophenol over nickel oxides, J. Mol. Catal, A 273 (2007) 303–309.

[53] Y. Xiaoyan, T. Xili, W. Jian, G. Changwei, Z. Mingang, L. Liping, Synthesis of mesoporous NiO nanoflake array and its enhanced electrochemical performance for supercapacitor application, J. Alloys Compd. 593 (2014) 184–189.

[54] K.S. Kim, R.E. Davis, Electron spectroscopy of the nickel oxygen system, J. Electron Spectrosc. Relat. Phenom. 1 (1972) 251–258.

[55] M.C. Biesinger, B.P. Payne, L.W.M. Lau, A. Gerson, R.S.C. Smart, X-ray photoelectron spectroscopic chemical state quantification of mixed nickel metal, oxide and hydroxide systems, Surf. Interface Anal. 41 (2009) 324–332.

[56] B. Zhao, X.K. Ke, J.H. Bao, C.L. Wang, L. Dong, Y.W. Chen, H.L. Chen, Synthesis of flower-like NiO and effects of morphology on its catalytic properties, J. Phys. Chem. C. 113 (2009) 14440–14447.

[57] Y. Hattori, T. Konishi, K. Kaneko, XAFS and XPS studies on the enhancement of methane adsorption by NiO dispersed ACF with the relevance to structural change of NiO, Chem. Phys. Lett. 355 (2002) 37–42.

[58] A.P. Grosvenor, M.C. Biesinger, R.S.C. Smart, N.S. McIntyre, New interpretations of XPS spectra of nickel metal and oxides, Surf. Sci. 600 (2006) 1771–1779.

[59] H.A.E.H. Weaver, J.F. Weaver, G.B. Hoflund, G.N. Salaita, Electron energy loss spectroscopic investigation of Ni metal and NiO before and after surface reduction by Ar+ bombardment, J. Electron Spectrosc. Relat. Phenom. 134 (2004) 139–171.

[60] A. Machocki, T. Ioannides, B. Stasinska, W. Gac, G. Avgouropoulos, D. Delimaris, W. Grzegorczyk, S. Pasieczna, Manganese lanthanum oxides modified with silver for the catalytic combustion of methane, J. Catal. 227 (2004) 282–296.

[61] C.C. Yu, Y.L. Chen, C.L. Hung, Surface chemistry of polyacrylonitrile and rayon based activated carbon fibers after post heat treatment, Mater. Chem. Phys. 101 (2007) 199–210.

[62] X. Wang, R. Zheng, Z. Liu, H. Ho, J. Xu, S.P. Ringer, Structural, optical and magnetic properties of Co-doped ZnO nanorods with hidden secondary phases, Nanotechnology 19 (2008) 455702-1–455702-8.

[63] G. Bai, H. Dai, J. Deng, Y. Liu, W. Qiu, Z. Zhao, X. Li, H. Yang, The micro emulsion preparation and high catalytic performance of mesoporous NiO nanorods and nanocubes for toluene combustion, Chem. Eng. J. 219 (2013) 200–208.

[64] M. Ahmad, E. Ahmed, Z.L. Hong, X.L. Jiao, T. Abbas, N.R. Khalid, Enhancement in visible light-responsive photocatalytic activity by embedding Cu-doped ZnO nanoparticles on multi-walled carbon nanotubes, Appl. Surf. Sci. 285 (2013) 702–712.

[65] C.M. Castilla, M.V.L. Ramon, F.C. Marin, Changes in surface chemistry of activated carbons by wet oxidation, Carbon 38 (2000) 1995–2001.

[66] T.I.T. Okpalugo, P. Papakonstantinou, H. Murphy, J. McLaughlin, N.M.D. Brown, High resolution XPS characterization of chemical functionalized MWCNTs and SWCNTs, Carbon 43 (2005) 153–161.

[67] D.J. Balazs, K. Triandafillu, Y. Chevolot, B.O. Aronsson, H. Harms, P. Descouts, H.J. Mathieu, Surface modification of PVC endotracheal tubes by oxygen discharge to reduce bacterial adhesion, Surf. Inter. Anal. 35 (2003) 301–309.

[68] W.H. Lee, S.J. Kim, W.J. Lee, J.G. Lee, R.C. Haddon, P.J. Reucroft, X-ray photoelectron spectroscopy studies of surface modified single walled carbon nanotube materials, Appl. Surf. Sci. 181 (2001) 121–127.

[69] M.T. Martinez, M.A. Callejas, A.M. Benito, M. Cochet, S. Seeger, A. Anson, J. Schreiber, Sensitivity of single wall carbon nanotubes to oxidative processing: Structural modification, intercalation and functionalization, Carbon 41 (2003) 2247–2256.

[70] B. Hapke, Theory of Reflectance and Emittance Spectroscopy, University Press, Cambridge, 1993.

[71] J. Liqiang, Q. Yichun, W. Baiqi, L. Shudan, J. Baojiang, Y. Libin, F. Wei, F. Honggang, S. Jiazhong, Review of photoluminescence performance of nano sized semiconductor materials and its relationships with photocatalytic activity, Sol. Energy Mater. Sol. Cells. 90 (2006) 1773–1787.

[72] C. Pan, R. Ding, Y. Hu, G. Yang, Electro spinning fabrication of rime like NiO nanowires/nano fibers hierarchical architectures and their photocatalytic properties, Physica E 54 (2013) 138–143.

[73] A. Hameed, T. Montini, V. Gombac, P. Fornasiero, Photocatalytic decolourization of dyes on NiO–ZnO nano-composites, Photochem. Photobiol. Sci. 8 (2009) 677–682.

[74] X.F. Song, L. Gao, Facile synthesis and hierarchical assembly of hollow nickel oxide architectures bearing enhanced photocatalytic properties, J. Phys. Chem. C 112 (2008) 15299–15305.

[75] S. Shang, K. Xue, D. Chen, X. Jiao, Preparation and characterization of rose like NiO nanostructures, CrystEngComm 13 (2011) 5094–5099.

[76] J.R. Utrilla, M.S. Polo, Ozonation of 1,3,6-naphthalenetrisulphonic acid catalysed by activated carbon in aqueous phase, Appl. Catal., B 39 (2002) 319–329.

[77] I.V. Gala, J.J.L. Penalver, M.S. Polo, J.R. Utrilla, Activated carbon as photocatalyst of reactions in aqueous phase, Appl. Catal., B 142–143 (2013) 694–704.

[78] H.P. Boehm, Free radicals and graphite, Carbon 50 (2012) 3154–3157.

[79] W.N.A. Guerra, J.M.T. Santos, L.R.R. Araujo, Decolorization and mineralization of reactive dyes by a photocatalytic process using ZnO and UV radiation, Water Sci. Technol. 66 (2012) 158–164.

[80] J.C. Luka, M. Klementova, P. Bezdick, S. Bakardijev, J. Subrt, L. Szatmary, Z. Bastl, J. Jirkovsky, Influence of Zr as TiO₂ doping ion on photocatalytic degradation of 4-chlorophenol, Appl. Catal., B 74 (2007) 83–91.

[81] J. Matos, J. Laine, J.M. Herrmann, Synergy effect in the photocatalytic degradation of phenol on a suspended mixture of titania and activated carbon, Appl. Catal., B 18 (1998) 281–291.

[82] M. Ahmad, E. Ahmed, Z.L. Hong, J.F. Xu, N.R. Khalid, A. Elhissi, W. Ahmed, A facile one-step approach to synthesizing ZnO/graphene composites for enhanced degradation of methylene blue under visible light, Appl. Surf. Sci. 274 (2013) 273–281.

[83] N.R. Khalid, Z.L. Hong, E. Ahmed, Y.W. Zhang, H. Chan, M. Ahmad, Synergistic effects of Fe and graphene on photocatalytic activity enhancement of TiO₂ under visible light, Appl. Surf. Sci. 258 (2012) 5827–5834.

[84] Y. Wang, Solar photocatalytic degradation of eight commercial dyes in TiO₂ suspension, Water Res. 34 (2000) 990–994.

[85] M. Kosmulski, pH-dependent surface charging and points of zero charge. IV: Update and new approach, J. Colloid. Interface Sci. 337 (2009) 439–448.

[86] W.Z. Tang, C.P. Huang, Photocatalyzed oxidation path ways of 2,4-dichlorophenol by CdS in basic and acidic aqueous solutions, Water Res. 29 (1995) 745–756.

[87] K. Baransi, Y. Dubowski, I. Sabbah, Synergetic effect between photocatalytic degradation and adsorption processes on the removal of phenolic compounds from olive mill wastewater, Water Res. 46 (2012) 789–798.

[88] J.C. D'Oliveria, G. AlSayyed, P. Pichat, Photodegradation of 2 and 3-chlorophenol in TiO₂ aqueous suspension, Environ. Sci. Technol. 24 (1990) 990–996.

[89] Z. Shu, X. Jiao, D. Chen, Hydrothermal synthesis and selective photocatalytic properties of tetragonal star like ZrO₂ nanostructures, CrystEngComm 15 (2013) 4288–4294.

[90] S.H. Yoon, J.H. Lee, Oxidation mechanism of As (lll) in the UV/TiO₂ system: Evidence for a direct hole oxidation mechanism, Environ. Sci. Technol. 39 (2005) 9695–9701.

[91] B. Bayarri, J. Gimenez, D. Curco, S. Esplugas, Photocatalytic degradation of 2,4-dichlorophenol by TiO₂/UV: Kinetics, actinometries and models, Catal. Today 101 (2005) 227–236.

[92] C.B. Mendive, D.W. Bahnemann, M.A. Blesa, Microscopic characterization of the photocatalytic oxidation of oxalic acid adsorbed onto TiO₂ by FTIR-ATR, Catal. Today 101 (2005) 237–244.

[93] L. Mansouri, L. Bousselmi, A. Ghrabi, Degradation of recalcitrant organic contaminants by solar photocatalysis, Water. Sci. Technol. 55 (2007) 119–125.

[94] E.L. Foletto, S. Battiston, J.M. Simoes, M.M. Bassaco, L.S.F. Pereira, E.M.M. Flores, E.I. Muller, Synthesis of ZnAl₂O₄ nanoparticles by different routes and the effect of its pore size on the photocatalytic process, Microporous Mesoporous Mater. 163 (2012) 29–33.